

Multiple magnetic topological phases in bulk van der Waals crystal MnSb_4Te_7

Shuchun Huan,^{1†} Shihao Zhang,^{1†} Zhicheng Jiang,^{2†} Hao Su¹, Hongyuan Wang,¹
Xin Zhang,¹ Yichen Yang,² Zhengtai Liu,² Xia Wang,^{1,4} Na Yu,^{1,4} Zhiqiang Zou^{1,4},
Dawei Shen^{2,5*}, Jianpeng Liu^{1,3*}, Yanfeng Guo^{1*}

¹ School of Physical Science and Technology, ShanghaiTech University, Shanghai
201210, China

² State Key Laboratory of Functional Materials for Informatics, Shanghai Institute of
Microsystem and Information Technology (SIMIT), Chinese Academy of Sciences,
Shanghai 200050, China

³ ShanghaiTech Laboratory for Topological Physics, Shanghai 201210, China

⁴ Analytical Instrumentation Center, School of Physical Science and Technology,
ShanghaiTech University, Shanghai 201210, China

⁵ Center of Materials Science and Optoelectronics Engineering, University of Chinese
Academy of Sciences, Beijing 100049, China

The magnetic van der Waals crystals $\text{MnBi}_2\text{Te}_4/(\text{Bi}_2\text{Te}_3)_n$ have drawn significant attention due to their rich topological properties and the tunability by external magnetic field. Although the $\text{MnBi}_2\text{Te}_4/(\text{Bi}_2\text{Te}_3)_n$ family have been intensively studied in the past few years, their close relatives, the $\text{MnSb}_2\text{Te}_4/(\text{Sb}_2\text{Te}_3)_n$ family, remain much less explored. In this work, combining magnetotransport measurements, angle-resolved photoemission spectroscopy, and first principles calculations, we find that MnSb_4Te_7 , the $n = 1$ member of the $\text{MnSb}_2\text{Te}_4/(\text{Sb}_2\text{Te}_3)_n$ family, is a magnetic topological system with versatile topological phases which can be manipulated by both carrier doping and magnetic field. Our calculations unveil that its A-type antiferromagnetic (AFM) ground state stays in a \mathbb{Z}_2 AFM topological insulator phase, which can be converted to an inversion-symmetry-protected axion insulator phase when in the ferromagnetic (FM) state. Moreover, when this system in the FM phase is

slightly carrier doped on either the electron or hole side, it becomes a Weyl semimetal with multiple Weyl nodes in the highest valence bands and lowest conduction bands, which are manifested by the measured notable anomalous Hall effect. Our work thus introduces a new magnetic topological material with different topological phases which are highly tunable by carrier doping or magnetic field.

[†]The authors contributed equally to this work.

*Corresponding authors:

dwshen@mail.sim.ac.cn,

liujp@shanghaitech.edu.cn,

guoyf@shanghaitech.edu.cn.

INTRODUCTION

Magnetic topological materials have roused a surge of interest in recent years due to their unconventional bulk transport properties [1-9], anomalous surface or edge states [10-22], and the coupling between the magnetic and electronic degrees of freedom, which allow for magnetic control of different topological phases [23-29]. The $\text{MnBi}_2\text{Te}_4/(\text{Bi}_2\text{Te}_3)_n$ family is a fertile ground to realize various magnetic topological phases such as axion insulators [25-27], Weyl semimetals (WSMs) [28-30], and quantum anomalous Hall (QAH) insulators [31, 32]. The crystal structure of the parent MnBi_2Te_4 is constructed by stacking the “Te-Bi-Te-Mn-Te-Bi-Te” septuple layers (SLs) along the c axis in a triangle lattice via van der Waals (vdW) interaction. MnBi_2Te_4 is a bulk topological insulator (TI) with a peculiar A-type antiferromagnetic (AFM) magnetic structure in which the in-plane exchange is ferromagnetic (FM) while the interlayer coupling is AFM [2,5,19,20,33]. This magnetic structure provides access to novel topological phases, such as the QAH effect observed in thin MnBi_2Te_4 flake with odd number of SLs under zero magnetic field [31] and an axion insulator state characterized by zero Hall plateau observed in six SLs MnBi_2Te_4 [25]. Moreover, the bulk $\text{MnBi}_2\text{Te}_4/(\text{Bi}_2\text{Te}_3)_n$ systems exhibit intriguing properties such as the unconventional topological surface states [15, 16, 18-20, 34-37], the complex magnetic phase diagram [27, 38], and the unusual transition behavior with Sb substitutions [39-42].

Although the $\text{MnBi}_2\text{Te}_4/(\text{Bi}_2\text{Te}_3)_n$ family have been extensively studied, many issues, such as the zero-field QAH effect and axion insulator state, are still waiting for verifications with more convincing evidences. In this regard, their close relatives, the $\text{MnSb}_2\text{Te}_4/(\text{Sb}_2\text{Te}_3)_n$ family, are definitely important and hopeful for the study of the unusual properties of magnetic topological systems. Previous first principles calculations indicate that pristine MnSb_2Te_4 is a topologically trivial insulator in both AFM and FM phases, and can be driven into a WSM under substantial compressive strain along the c axis [43], or into a FM TI by the application of external magnetic

field [44]. In this work, for the first time we report the successful synthesis of high-quality single crystal MnSb_4Te_7 , a member of the $\text{MnSb}_2\text{Te}_4/(\text{Sb}_2\text{Te}_3)_n$ family with $n = 1$, and demonstrate that it exhibits versatile magnetic topological phases based on magnetotransport measurements, first principles calculations, and angle-resolved photoemission spectroscopy (ARPES). Each MnSb_4Te_7 primitive cell consists of a MnSb_2Te_4 SL intercalated with an additional Sb_2Te_3 quintuple layer (QL) as shown in Figure 1(a). The local magnetic moments contributed by the d orbitals of Mn^{2+} ions form long range FM ordering within the SL plane, and the magnetic moments from neighboring SLs are antiferromagnetically ordered along the c axis, establishing the similar A-type AFM state as that of MnBi_2Te_4 , shown schematically in Figure 1(a). The AFM interlayer exchange is weaker compared with that in MnSb_2Te_4 due to the Sb_2Te_3 QL intercalation, which results in a lower Néel temperature $T_N = 13.5$ K. First principles calculations indicate that MnSb_4Te_7 in the AFM phase is an axion insulator protected by the combination of time-reversal (\mathcal{T}) and half lattice translation symmetries ($\tau_{1/2}$), which is associated with gapped topological surface states. Such a phase is also known as a \mathbb{Z}_2 AFM topological insulator. The interlayer AFM ordering can be converted into FM ordering under very small vertical magnetic field $\mu_0 H > 0.15$ T, and then MnSb_4Te_7 becomes a FM axion insulator protected by inversion symmetry. Moreover, the system in the FM phase would become a WSM upon slight electron or hole doping, which is characterized by notable anomalous Hall effect (AHE) caused by multiple Weyl nodes in the lowest conduction bands and highest valence bands. Our work indicates that MnSb_4Te_7 is a promising magnetic topological material exhibiting both axion-insulator and Weyl-semimetal phases, which can be tuned by both magnetic field and carrier doping.

The details for crystal growth, magnetization, magnetotransport, ARPES measurements, and first principles calculations of the bulk MnSb_4Te_7 are presented in Supplementary Information (SI).

RESULTS AND DISCUSSION

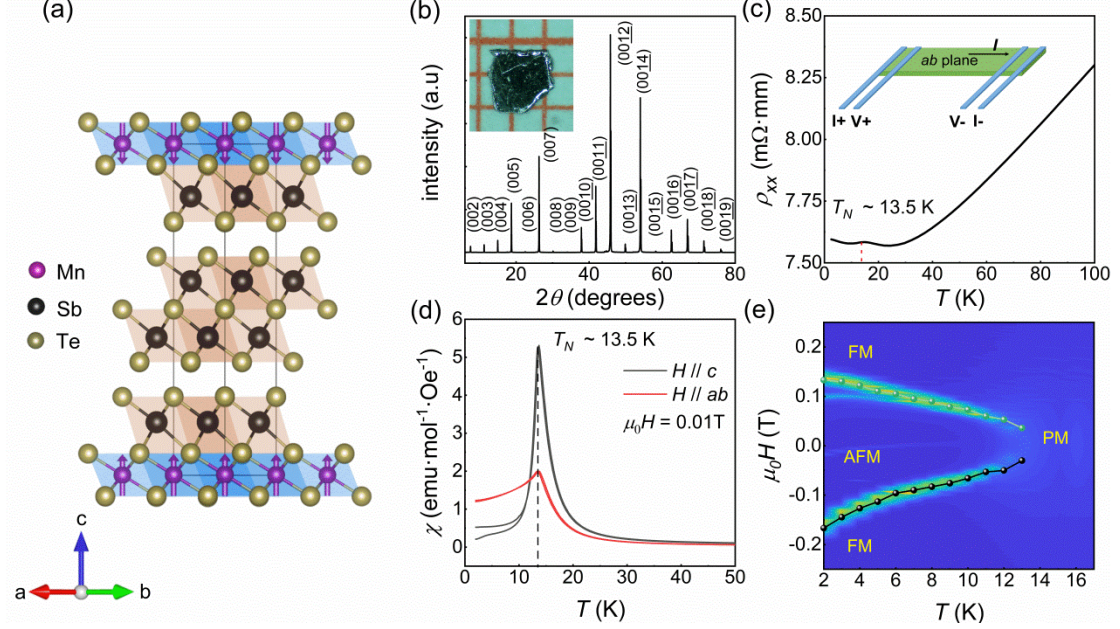


Fig. 1. (a) The schematic crystal structure of MnSb_4Te_7 . The blue arrows represent the Mn^{2+} spins in the A-type AFM structure. Green block: edge-sharing SbTe_6 octahedra. Blue block: edge-sharing MnTe_6 octahedra. (b) The room temperature powder X-ray diffraction peaks from the ab plane of MnSb_4Te_7 crystal. Insert: Image of a typical MnSb_4Te_7 single crystal synthesized in this work. (c) The temperature dependent of transverse resistivity ρ_{xx} at $\mu_0 H = 0$ T measured from 2 K to 100 K. The sketch for the four-probe measurements configuration is inserted. (d) The temperature dependence of susceptibility χ under $\mu_0 H = 0.01$ T for $H // c$ and $H // ab$ plane. (e) The magnetic phase diagram of MnSb_4Te_7 . The solid dots and line with solid dots represent the critical magnetic fields as a function of temperature.

Figure 1(b) shows the room temperature Bragg reflections from the ab plane of a typical MnSb_4Te_7 single crystal, which can be nicely indexed by using the MnBi_4Te_7 structure model. A picture of a typical MnSb_4Te_7 single crystal is shown as an insert of Figure 1(b), with the dimensions of about $2 \times 2 \times 0.2 \text{ mm}^3$ and the flat surface corresponding to the ab plane.

The resistivity and magnetic properties of MnSb_4Te_7 are depicted in Figures 1(c)-(e), respectively. Seen from the temperature dependence of longitudinal resistivity ρ_{xx} at $\mu_0 H = 0$ T with $I // ab$ plane presented in Figure 1(c), it decreases linearly with decreasing the temperature to ~ 25 K, and then slightly increases below 20 K upon further cooling. The slight upturn of ρ_{xx} at low temperature likely originates from the enhanced scattering amplitudes due to the critical magnetic fluctuations approaching the Néel temperature, which is commonly observed in low dimensional magnetic systems. An abrupt drop of ρ_{xx} is observed at 13.5 K, consistent with the AFM ordering temperature manifested by the magnetic susceptibility presented in Figure 1(d). Seen in both zero-field-cooled (ZFC) and field-cooled (FC) curves measured at $\mu_0 H = 0.01$ T with $H // c$ axis and $H // ab$ plane, respectively, abrupt transitions around $T_N = 13.5$ K are visible, indicating an intrinsic long range AFM ordering, which is similar to that observed in MnBi_4Te_7 [6,9,25]. The magnetic susceptibility decreases dramatically below T_N for $H // c$, but only slightly decreases for $H // ab$, unveiling an anisotropic AFM exchange with the c axis being the magnetic easy axis. When H is set along the c axis, the ZFC and FC curves are slightly separated from each other, implying possible hysteresis behavior [See details in Figure S2]. The weak interlayer AFM coupling can be easily converted into FM order by vertical magnetic field. The critical magnetic fields for such AFM-FM transition as a function of temperature are marked by the blue (for positive H) and black (for negative H) dots in Figure 1(e), which decreases with increasing temperature. Eventually the system enters the paramagnetic phase for $T > T_N$, as marked by “PM” in Figure 1(e).

The MnSb_4Te_7 system obeys the symmetries of $P-3m1$ space group, which include inversion symmetry (inversion center is located at the Mn atom) as shown Figure 1(a). First principles calculations are employed to investigate the electronic structure of MnSb_4Te_7 with four different magnetic structures. The detailed methods can be found in the SI. First, we investigate the AFM ground state. Figure 2(a) reveals

that the MnSb_4Te_7 in the AFM structure has a direct gap of 75 meV. When the system is in the FM structures, the bulk systems have indirect gaps around 60 meV as shown in Figures 2(b)-2(d), for the FM magnetizations pointing along z , x , and y directions, respectively. The three FM phases with magnetizations pointing along x , y , and z directions are denoted by “FMx”, “FMy” and “FMz” in the following discussions. The energy bands near the Fermi level are mainly contributed by the Sb p and Te p orbitals with substantial spin-orbit coupling (SOC). The localized $3d$ orbitals from the Mn^{2+} ions contribute to the local magnetic moments, which are coupled to the conduction electrons through effective Zeeman couplings, thus combining SOC with magnetism in the electronic degrees of freedom and enabling the realization of different magnetic topological phases in the system.

Table I. The symmetries of bulk MnSb_4Te_7 in different magnetic states.

	P	$\mathcal{T}\tau_{1/2}$	M_x	C_{3z}	C_{2x}
AFM	✓	✓	✗	✓	✗
FMx	✓	✗	✓	✗	✓
FMy	✓	✗	✗	✗	✗
FMz	✓	✗	✗	✓	✗

The bulk MnSb_4Te_7 crystal in the non-magnetic phase has P , M_x , C_{3z} , and C_{2x} symmetries. The AFM state doubles the primitive cell along the c axis, which breaks the M_x and C_{2x} , but preserves P symmetry and an additional non-symmorphic symmetry which combines \mathcal{T} and $\tau_{1/2}$. Inversion symmetry is also preserved in all the FMx, FMy, and FMz phases. The symmetries of bulk MnSb_4Te_7 with the four different magnetic configurations are enumerated in Table I.

Because the MnSb_4Te_7 system preserves inversion symmetry in all the four

magnetic configurations, we can use the symmetry indicator \mathbb{Z}_4 invariant to characterize the topological characters of the different magnetic topological phases [45-48]. Here the \mathbb{Z}_4 invariant can be defined as $\mathbb{Z}_4 = \sum_{k=1}^8 (n_k^+ - n_k^-) / 2 \text{ mod } 4$, where n_k^+ / n_k^- is the number of occupied states with even/odd parity at the inversion-invariant momenta \mathbf{k} . $\mathbb{Z}_4 = 1$ or 3 indicates a WSM phase, while $\mathbb{Z}_4 = 2$ means that the system is an axion insulator given that the Chern numbers on all the 2D \mathbf{k} planes in the Brillouin zone are zeros. The parity analysis reveals that all these magnetic states are axion insulators with quantized bulk orbital magnetoelectric coupling and gapped topological surface states [49-54], and the parities of the occupied bands at the inversion-invariant \mathbf{k} points are shown in Table. S2 of the SI. The hybrid Wannier charge center evolution (also known as the “Wilson loops”) [55, 56] in the four magnetic states in the $k_z = 0$ plane also indicates that the system in different magnetic configurations exhibits nontrivial topological properties as characterized by the winding pattern of the Wilson loops, which are shown in Figure S5 of SI. It is worthwhile to note that in addition to inversion symmetry, MnSb_4Te_7 in the AFM phase also has $\mathcal{J}\tau_{1/2}$ symmetry, which allows for a \mathbb{Z}_2 classification. Thus, MnSb_4Te_7 in the AFM phase can also be classified as a \mathbb{Z}_2 AFM TI [57]. Different from the MnBi_2Te_4 system which only stays in the axion-insulator state in the AFM configuration but becomes a WSM in the FM configuration [23,27], MnSb_4Te_7 system retains the robust axion-insulator state regardless of magnetic ordering or magnetic orientation. More interestingly, in the FM configurations the MnSb_4Te_7 system behaves as a WSM upon slight electron or hole doping, because there are multiple Weyl nodes in the lowest conduction bands and highest valence bands, and the positions of these Weyl nodes can be moved by changing the magnetization direction. Such WSM phase introduced by carrier doping will be discussed in detail in the following. We see that the MnSb_4Te_7 system in the FM configurations realizes a unique phase with co-existing axion-insulator and Weyl-semimetal states, the transition between which can be electrically tuned by slight carrier doping.

The MnSb_4Te_7 system has two types of surface terminations on the (001) plane: MnSb_2Te_4 SLs and Sb_2Te_3 QLs. Our calculation results shown in Figure S6 of SI indicate that there is a Dirac-like crossing near the Fermi level (E_F) in the spectrum of surface states with SL termination, but it becomes parabolic energy bands with larger band gap when the termination turns to the QL termination. This is similar to what has been observed in MnBi_4Te_7 [12,14,15,34]: the first type of surface states with SL termination are genuine Dirac surface states which are gapped out due to the Zeeman coupling to the surface magnetizations; while the second type of surface states with QL termination results from the hybridization between the states in the QLs and SLs. More details about the calculated surface states of MnSb_4Te_7 can be found in SI.

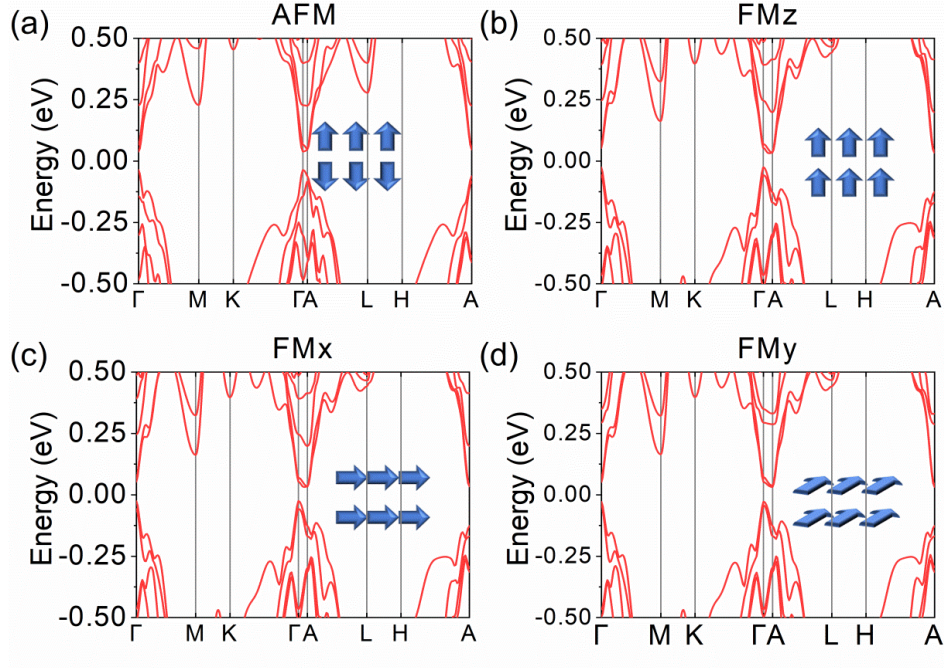


Fig. 2. The band structures of (a) A-type AFM state, (b) FM state with spin aligned along z direction (FMz), (c) FM state with x -direction spin (FMx), and (d) FM state with y -direction spin (FMy) of bulk MnSb_4Te_7 with considering the spin-orbital coupling effect. Here Fermi levels are set to zero and spin directions are remarked by blue arrows.

We continue to discuss the magnetotransport properties of MnSb_4Te_7 in different magnetic configurations. The synthesized bulk MnSb_4Te_7 crystals are slightly hole

doped which behave as metals in transport. Figure 3(a) shows the magnetic field H dependence of $\rho_{xx}(H)$. The AFM states are manifested by the resistivity plateaus for

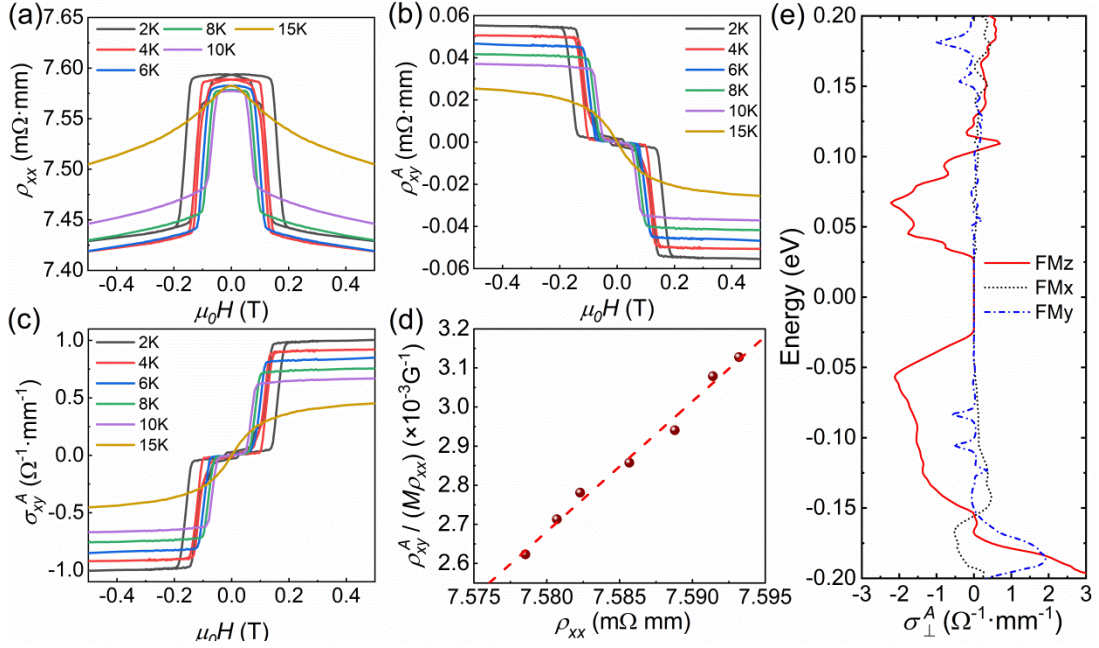


Fig. 3. (a) Magnetoresistance ρ_{xx} with $I \parallel ab$ plane and $H \parallel c$ at various temperatures. (b) The anomalous hall resistivity ρ_{xy}^A . (c) The anomalous hall conductivity σ_{xy}^A at various temperatures. (d) The plot of $\rho_{xy}^A / (M\rho_{xx})$ vs. ρ_{xx} . (e) The calculated anomalous Hall conductivities of MnSb_4Te_7 for the three different ferromagnetic states as a function of varied Fermi energy, where the actual Fermi energy is set as zero.

weak magnetic fields $H < H_c$ ($\mu_0 H_c \sim 0.1 - 0.2$ T) at temperatures lower than T_N . Spin-flop transitions are observed for $H > H_c$ and $T < T_N$, as characterized by the abrupt drop of ρ_{xx} when $H > H_c$, which is in good accordance with the previous magnetization measurements that suggest an AFM-FM transition at H_c . When the magnetic field is further enhanced, ρ_{xx} is slightly decreased implying that the local moments of the Mn^{2+} ions are fully saturated. The field dependence of the anomalous Hall resistivity ρ_{xy}^A is displayed in Figure 3(b). Clearly, when $T < T_N$ and $H > H_c$, the MnSb_4Te_7 system exhibits significant AHE with notable hysteresis loops shown in Figure 3(b). The magnitude of ρ_{xy}^A , the area of the hysteresis loops, and the

magnetization $M(H)$ all gradually diminish with the increase of temperature for $H > H_c$ and $T < T_N$, and they eventually (almost) vanish for $T > T_N$ (see details in Figure S2 of SI). The converted anomalous Hall conductivity (AHC) $\sigma_{xy}^A (= -\rho_{xy}^A / (\rho_{xy}^A{}^2 + \rho_{xx}^2))$ is presented in Figure 3(c). To determine the dominant mechanism for the AHC, the ρ_{xy}^A vs. ρ_{xx} relationship is fitted using the method described in Ref. [1]. As shown in Figure 3(d), $\rho_{xy}^A / (M\rho_{xx})$ is linearly dependent on ρ_{xx} when $\rho_{xx} < 7.6$ m Ω mm, suggesting that the dominant contribution to AHC in MnSb₄Te₇ is from the intrinsic Berry curvatures of the band structures. At 2 K, ρ_{xy}^A is extracted to be 54 $\mu\Omega$ ·mm and σ_{xy}^A is 0.99 Ω^{-1} mm⁻¹, which is rather close to the theoretical value 1.12 Ω^{-1} mm⁻¹ as discussed in detail later. It should be noted that the low temperature upturn of ρ_{xx} is possibly due to slightly enhanced electron-electron interactions [58, 59], which does not change the intrinsic nature of the AHE.

We also have calculated the AHC of the three FM phases of MnSb₄Te₇ with $151 \times 151 \times 151$ k -points mesh as shown in Figure 3(e). Near the E_F , the AHC of FMz state is larger than those of the other two FM states. It should be noted that the calculated AHC component is always in the plane perpendicular to the magnetization direction. When the system is slightly hole doped, there are four Weyl nodes of FMx state in the -0.15 ~ 0 eV range located at $\pm(\pm 0.003, 0.049, 0.066)$ ang⁻¹ (0 is set to be the middle of the energy gap), while there are only two Weyl nodes in the FMz state in the same energy range located at $\pm(-0.003, 0.049, 0.066)$ ang⁻¹ due to the lack of M_x mirror symmetry in FMz phase. The four Weyl nodes of FMx state are almost in the $k_x = 0$ plane, thus contribute little to the yz component of the AHC. But the Weyl nodes of FMz state are well separated from the $k_z = 0$ plane, so we can see the remarkable AHC σ_{xy}^A compared to other magnetic states.

To confirm the non-trivial topological properties of MnSb₄Te₇, we used the synchrotron-based ARPES to probe its low-energy band structure, as shown in Figure

4. By changing the photon energy in an extensive range of 50 ~ 90 eV, which covers more than one whole Brillouin zone, we can distinguish unaltered Dirac surface states from the bulk ones, as marked by red arrows in Figure 4 (a). These ARPES spectra demonstrate the prominent p-type carrier dosage in MnSb_4Te_7 . Through detailed comparison with the calculated band dispersion along the Γ -K direction [Figure 4(b)], we can evaluate that the Fermi level of the as-grown MnSb_4Te_7 is located ~180 meV below the Dirac point (DP), as illustrated in Figure 4(c). We note that the calculated σ_{xy}^A based on this estimation of E_F is $1.12 \Omega^{-1}\cdot\text{mm}^{-1}$, which is in remarkable agreement with the transport result taken at 2 K ($0.99 \Omega^{-1}\cdot\text{mm}^{-1}$). To further observe the Dirac surface states, we tried to tune its chemical potential by Bi substitution for Sb in MnSb_4Te_7 . As shown in Figure 4(d), with ~15% Bi substitution, the E_F of $\text{Mn}(\text{Bi}_{0.15}\text{Sb}_{0.85})_4\text{Te}_7$ is discovered to shift up by ~120 meV, while leaving the main band dispersion unchanged. Furthermore, we can extrapolate the Dirac band to its apex to obtain the position of DP, which is only 60 ± 10 meV above E_F , in line with our previous estimation for as-grown MnSb_4Te_7 . Potassium surface doping has been tried as well, while the chemical potential does not show significant movement, which might be attributed to the large density of states close to E_F (see details in Figure S10). In addition, can further prove the existence of a surface Dirac cone in the vicinity of E_F .

The Dirac cone is further shown by constant-energy cuts of $\text{Mn}(\text{Bi}_{0.15}\text{Sb}_{0.85})_4\text{Te}_7$ [Figure 4(e)]. Also, the experimental petal-like Fermi surface is in a good agreement with the calculation for SL termination [Figure S8(a)]. Nevertheless, MnSb_4Te_7 is expected to expose two kinds of terminations after cleaving, namely SL (MnSb_2Te_4) and QL (Sb_2Te_3). We have well scanned the whole sample cleaved surface with our $30 \mu\text{m} \times 30 \mu\text{m}$ synchrotron beam, while we could not distinguish between these two terminations, which is distinct from the case of MnBi_4Te_7 [14, 15, 34]. This might result from their rather similar band structure below the Dirac point according to our

calculations [Figure S8 of SI]. Moreover, similar to MnBi_4Te_7 , we as well find a dispersionless feature with 90 eV photons at the binding energy of ~ 3 eV, corresponding to the contributions of Mn 3d-states (Figure S9).

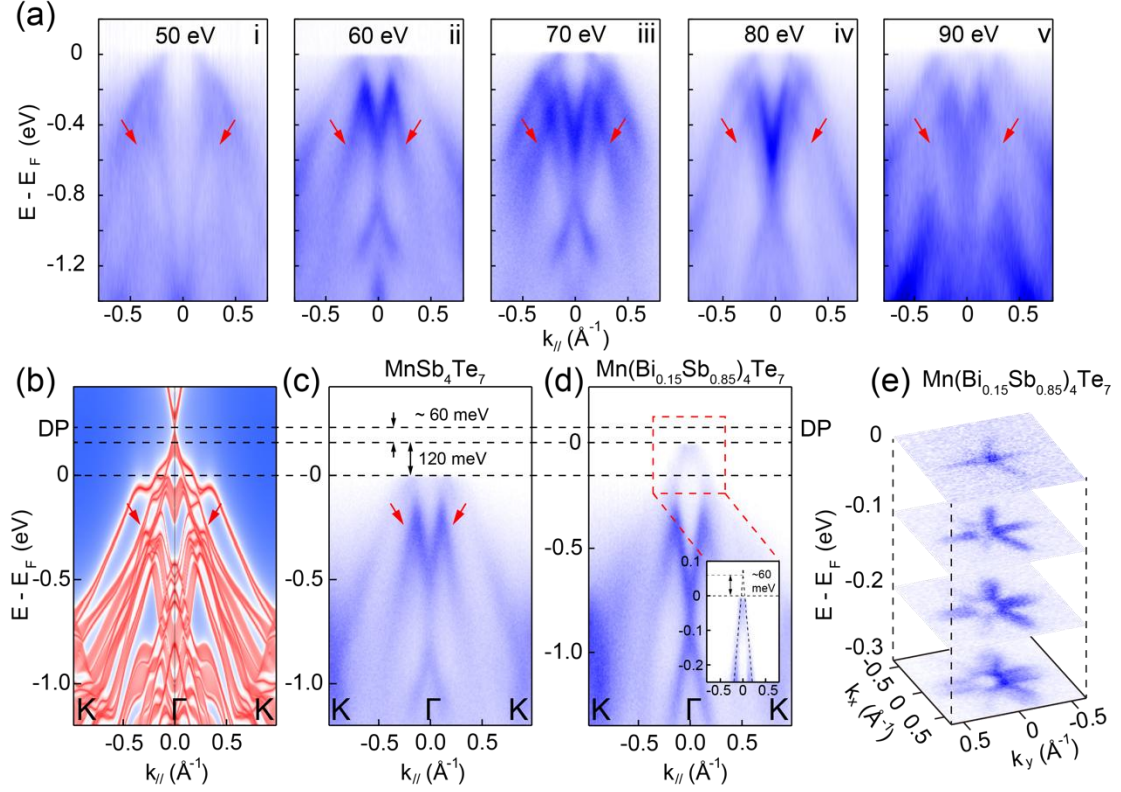


Fig. 4. (a) ARPES intensity plot along the Γ -K direction measured at $h\nu = 50, 60, 70, 80$ and 90 eV at 15 K. (b) Calculated band structure along Γ -K direction of SL termination. ARPES intensity mapped along the Γ -K direction of (c) MnSb_4Te_7 and (d) $\text{Mn}(\text{Bi}_{0.15}\text{Sb}_{0.85})_4\text{Te}_7$ collected at 60 eV. (e) Constant-energy surface of the Dirac cone cut for $\text{Mn}(\text{Bi}_{0.15}\text{Sb}_{0.85})_4\text{Te}_7$.

SUMMARY

To summarize, in this work we report the first successful growth of high-quality MnSb_4Te_7 single crystal, and have studied its magnetic topological properties combining transport measurements, first principles calculations, and ARPES studies.

We deduce that bulk MnSb_4Te_7 would stay in axion-insulator states for both FM and AFM configurations, which are associated with topologically nontrivial surface states that are confirmed by our ARPES measurements. Moreover, there are multiple Weyl nodes in the highest valence bands and lowest conduction bands in the FM phase such that the system behaves as a Weyl semimetal upon slight carrier doping, which is characterized by notable anomalous Hall effect. Therefore, the MnSb_4Te_7 in the FM configuration realizes a unique phase with co-existing axion-insulator and Weyl-semimetal states, and the transition between the two topological states can be tuned by carrier doping. Our work is a significant step forward in understanding the intriguing physical properties of magnetic topological materials, and will provide useful guidelines for future experimental and theoretical studies in this field.

ACKNOWLEDGEMENTS

The authors acknowledge the support by the Major Research Plan of the National Natural Science Foundation of China (No. 92065201), the National Natural Science Foundation of China (Grant Nos. 11874264 and U2032208), and the National Key R&D Program of the MOST of China (Grant No. 2016YFA0300204). S. Zhang and J. Liu acknowledge the start-up grant of ShanghaiTech University and the National Key R & D program of China (grant no. 2020YFA0309601). Y. F. Guo acknowledges the start-up grant of ShanghaiTech University and the Program for Professor of Special Appointment (Shanghai Eastern Scholar). Part of this research used Beamline 03U of the Shanghai Synchrotron Radiation Facility, which is supported by ME2 project under contract No. 11227902 from National Natural Science Foundation of China. The authors also thank the support from the Analytical Instrumentation Center (SPST-AIC10112914), SPST, ShanghaiTech University.

Reference

- [1] Q. Wang, Y. Xu, R. Lou, Z. Liu, M. Li, Y. Huang, D. Shen, H. Weng, S. Wang, and H. Lei, *Nat. Commun.* **9**, 3681 (2018).
- [2] M. Ikhlas, T. Tomita, T. Koretsune, M.-T. Suzuki, D. Nishio-Hamane, R. Arita, Y. Otani, and S. Nakatsuji, *Nat. Phys.* **13**, 1085 (2017).
- [3] S. Nakatsuji, N. Kiyohara, and T. Higo, *Nature* **527**, 212 (2015).
- [4] L. Xu, X. Li, L. Ding, T. Chen, A. Sakai, B. Fauqu é S. Nakatsuji, Z. Zhu, and K. Behnia, *Phys. Rev. B* **101**, 180404(R) (2020).
- [5] A. K. Nayak, J. E. Fischer, Y. Sun, B. Yan, J. Karel, A. C. Komarek, C. Shekhar, N. Kumar, W. Schnelle, J. Kubler, C. Felser, and S. S. Parkin, *Sci. Adv.* **2**, e1501870 (2016).
- [6] M. Z. Shi, B. Lei, C. S. Zhu, D. H. Ma, J. H. Cui, Z. L. Sun, J. J. Ying, and X. H. Chen, *Phys. Rev. B* **100**, 155144 (2019).
- [7] C.-Z. Chang, *et al.* *Science* **340**, 167 (2013).
- [8] M. Mogi, M. Kawamura, A. Tsukazaki, R. Yoshimi, K. S. Takahashi, M. Kawasaki, and Y. Tokura, *Sci. Adv.* **3**, eaao1669 (2017).
- [9] D. Xiao, J. Jiang, J.-H. Shin, W. Wang, F. Wang, Y.-F. Zhao, C. Liu, W. Wu, M. H. W. Chan, N. Samarth, and C.-Z. Chang, *Phys. Rev. Lett.* **120**, 056801 (2018).
- [10] L. Ye, M. Kang, J. Liu, F. von Cube, C. R. Wicker, T. Suzuki, C. Jozwiak, A. Bostwick, E. Rotenberg, D. C. Bell, L. Fu, R. Comin, and J. G. Checkelsky, *Nature* **555**, 638 (2018).
- [11] N. Morali, R. Batabyal, P. K. Nag, E. Liu, Q. Xu, Y. Sun, B. Yan, C. Felser, N. Avraham, and H. Beidenkopf, *Science* **365**, 1286 (2019).
- [12] L. Xu, *et al.* *Sci. Bull.* **65**, 2086 (2020).
- [13] Y.-J. Hao, *et al.* *Phys. Rev. X* **9**, 041038 (2019).
- [14] X. Wu, *et al.* *Phys. Rev. X* **10**, 031013 (2020).
- [15] R. C. Vidal, *et al.* *Phys. Rev. X* **9**, 041065 (2019).
- [16] Y. J. Chen, *et al.* *Phys. Rev. X* **9**, 041040 (2019).
- [17] D. Nevola, H. X. Li, J. Q. Yan, R. G. Moore, H. N. Lee, H. Miao, and P. D. Johnson, *Phys. Rev. Lett.* **125**, 117205 (2020).
- [18] Y. Gong, *et al.* *Chin. Phys. Lett.* **36**, 076801 (2019).
- [19] H. Li, *et al.* *Phys. Rev. X* **9**, 041039 (2019).
- [20] M. M. Otrokov, *et al.* *Nature* **576**, 416 (2019).
- [21] E. D. L. Rienks, *et al.* *Nature* **576**, 423 (2018).
- [22] K. N. Gordon, H. Sun, C. Hu, A. G. Linn, H. Li, Y. Liu, P. Liu, S. Mackey, Q. Liu, N. Ni, and D. Dessau, *arxiv:1910.13943* (2019).
- [23] C. Liu, Y. Wang, H. Li, Y. Wu, Y. Li, J. Li, K. He, Y. Xu, J. Zhang, and Y. Wang, *Nat. Mater.* **19**, 522 (2020).
- [24] D. Zhang, M. Shi, T. Zhu, D. Xing, H. Zhang, and J. Wang, *Phys. Rev. Lett.* **122**, 206401 (2019).
- [25] C. Hu, *et al.* *Sci. Adv.* **6**, eaba4275 (2020).
- [26] M. M. Otrokov, I. P. Rusinov, M. Blanco-Rey, M. Hoffmann, A. Y. Vyazovskaya,

- S. V. Eremeev, A. Ernst, P. M. Echenique, A. Arnau, and E. V. Chulkov, *Phys. Rev. Lett.* **122**, 107202 (2019).
- [27] J. Li, C. Wang, Z. Zhang, B.-L. Gu, W. Duan, and Y. Xu, *Phys. Rev. B* **100**, 121103 (2019).
- [28] T. Suzuki¹, L. Savary, J.-P. Liu, J. W. Lynn, L. Balents, and J. G. Checkelsky, *Science* **365**, 377 (2019).
- [29] J. Liu and L. Balents, *Phys. Rev. Lett.* **119**, 087202 (2017).
- [30] J. Li, Y. Li, S. Du, Z. Wang, B. L. Gu, S. C. Zhang, K. He, W. Duan, and Y. Xu, *Sci Adv* **5**, eaaw5685 (2019).
- [31] Y. Deng, Y. Yu, M. Z. Shi, Z. Guo, Z. Xu, J. Wang, X. H. Chen, and Y. Zhang, *Science* **367**, 895 (2020).
- [32] H. Deng, Z. Chen, A. Wołoś, M. Konczykowski, K. Sobczak, J. Sitnicka, I. V. Fedorchenko, J. Borysiuk, T. Heider, Ł. Pluciński, K. Park, A. B. Georgescu, J. Cano, and L. Krusin-Elbaum, *Nat. Phys.* **17**, 36 (2020).
- [33] J.-Q. Yan, Q. Zhang, T. Heitmann, Z. Haung, K. Y. Chen, J.-G. Cheng, W. Wu, D. Vaknin, B. C. Sales, and R. J. McQueeney, *Phys. Rev. Mater.* **3**, 064202 (2019).
- [34] C. Hu, K. N. Gordon, P. Liu, J. Liu, X. Zhou, P. Hao, D. Narayan, E. Emmanouilidou, H. Sun, Y. Liu, H. Brawer, A. P. Ramirez, L. Ding, H. Cao, Q. Liu, D. Dessau, and N. Ni, *Nat. Commun.* **11**, 97 (2020).
- [35] J. Wu, F. Liu, M. Sasase, K. Ienaga, Y. Obata, R. Yukawa, K. Horiba, H. Kumigashira, S. Okuma, T. Inoshita, and H. Hosono, *Sci. Adv.* **5**, eaax9989 (2019).
- [36] M. M. Otrokov, *et al.*, *Nature* **576**, 416 (2019).
- [37] N.-H. Jo, L.-L. Wang, R.-J. Slager, J. Q. Yan, Y. Wu, K. Lee, B. Schruck, A. Vishwanath, and A. Kaminski, *Phys. Rev. B* **102**, 045130 (2020).
- [38] I. I. Klimovskikh, *et al.* *npj Quantum Materials* **5**, 54 (2020).
- [39] B. Chen, F. Fei, D. Zhang, B. Zhang, W. Liu, S. Zhang, P. Wang, B. Wei, Y. Zhang, Z. Zuo, J. Guo, Q. Liu, Z. Wang, X. Wu, J. Zong, X. Xie, W. Chen, Z. Sun, S. Wang, Y. Zhang, M. Zhang, X. Wang, F. Song, H. Zhang, D. Shen, and B. Wang, *Nat. Commun.* **10**, 4469 (2019).
- [40] J. Q. Yan, S. Okamoto, M. A. McGuire, A. F. May, R. J. McQueeney, and B. C. Sales, *Phys. Rev. B* **100**, 104409 (2019).
- [41] W. Ko, M. Kolmer, J. Yan, A. D. Pham, M. Fu, F. Lüpke, S. Okamoto, Z. Gai, P. Ganesh, and A.-P. Li, *Phys. Rev. B* **102**, 115402 (2020).
- [42] C. Hu, S. Mackey, N. Ni, *arXiv:2008.09097*.
- [43] L. Q. Zhou, Z. Y. Tan, D. Y. Yan, Z. Fang, Y. G. Shi, and H. M. Weng, *Phys. Rev. B* **102**, 085114 (2020).
- [44] S. Wimmer, J. Sánchez-Barriga, P. Küppers, A. Ney, E. Schierle, F. Freyse, O. Caha, J. Michalicka, M. Liebmann, D. Primetzhofer, M. Hoffmann, A. Ernst, M. M. Otrokov, G. Bihlmayer, E. Weschke, B. Lake, E. V. Chulkov, M. Morgenstern, G. Bauer, G. Springholz, O. Rader, *arXiv:2011.07052*.
- [45] J. Kruthoff, J. Boer, J. Wezel, C. L. Kane, and R. -J. Slager, *Phys. Rev. X* **7**, 041069 (2017).
- [46] H. Watanabe, H. C. Po, and A. Vishwanath, *Sci. Adv.* **4**, eaat8685 (2018).

- [47] S. Ono and H. Watanabe, Phys. Rev. B **98**, 115150 (2018).
- [48] Y. Xu, Z. Song, Z. Wang, H. Weng, and X. Dai, Phys. Rev. Lett. **122**, 256402 (2019).
- [49] X.-L. Qi, T. L. Hughes, and S.-C. Zhang, Phys. Rev. B **78**, 195424 (2008).
- [50] A. M. Essin, J. E. Moore, and D. Vanderbilt, Phys. Rev. Lett. **102**, 146805 (2009).
- [51] A. M. Turner, Y. Zhang, R. S. K. Mong, and A. Vishwanath, Phys. Rev. B **85**, 165120 (2012).
- [52] A. M. Essin, A. M. Turner, J. E. Moore, and D. Vanderbilt, Phys. Rev. B **81**, 205104 (2010).
- [53] A. Malashevich, I. Souza, S. Coh, and D. Vanderbilt, New J. Phys. **12**, 053032 (2010).
- [54] N. Varnava and D. Vanderbilt, Phys. Rev. B **98**, 245117 (2018).
- [55] A. Soluyanov and D. Vanderbilt, Phys. Rev. B **83**, 235401 (2011).
- [56] R. Yu, X. L. Qi, A. Bernevig, Z. Fang, and X. Dai, Phys. Rev. B **84**, 075119 (2011).
- [57] R. S. K. Mong, A. M. Essin, and J. E. Moore, Phys. Rev. B **81**, 245209 (2010).
- [58] G. Shi, et al. Chin. Phys. Lett. **37**, 047301 (2020).
- [59] P. Hosur, S. A. Parameswaran, and A. Vishwanath, Phys. Rev. Lett. **108**, 046602 (2012).

Supplementary Information

Multiple magnetic topological phases in bulk van der Waals crystal MnSb_4Te_7

Shuchun Huan,^{1†} Shihao Zhang,^{1†} Zhicheng Jiang,^{2†} Hao Su¹, Hongyuan Wang,¹
Xin Zhang,¹ Yichen Yang,² Zhengtai Liu,² Xia Wang,^{1,4} Na Yu,^{1,4} Zhiqiang Zou^{1,4},
Dawei Shen^{2,5*}, Jianpeng Liu^{1,3*}, Yanfeng Guo^{1*}

¹ School of Physical Science and Technology, ShanghaiTech University, Shanghai
201210, China

² State Key Laboratory of Functional Materials for Informatics, Shanghai Institute
of Microsystem and Information Technology (SIMIT), Chinese Academy of Sciences,
Shanghai 200050, China

³ ShanghaiTech Laboratory for Topological Physics, Shanghai 201210, China

⁴ Analytical Instrumentation Center, School of Physical Science and Technology,
ShanghaiTech University, Shanghai 201210, China

⁵ Center of Materials Science and Optoelectronics Engineering, University of Chinese
Academy of Sciences, Beijing 100049, China

[†]These authors contributed equally to this work.

*Corresponding authors:

dwshen@mail.sim.ac.cn,

liujp@shanghaitech.edu.cn,

guoyf@shanghaitech.edu.cn.

a. Crystal growth and characterizations

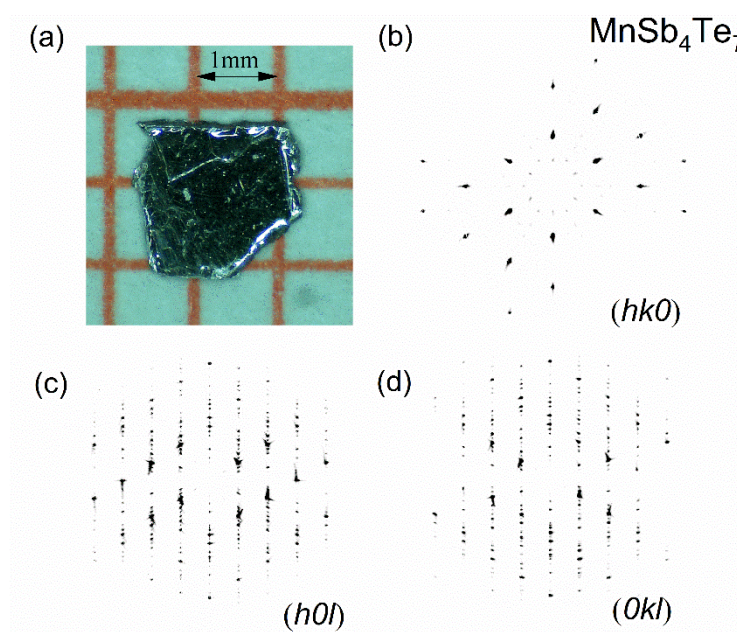


Fig. S1. (a) A typical picture for obtained MnSb₄Te₇ single crystal. (b) – (c) Single crystal X-ray diffraction patterns in the reciprocal space along the $(0kl)$, $(h0l)$ and $(hk0)$ directions for MnSb₄Te₇ measured at 298 K.

The MnSb₄Te₇ single crystals were grown by using the self-flux method. Starting materials of Mn (99.95%, aladdin), Sb (99.999%, aladdin) and Te (99.9999%, aladdin) blocks were mixed in a molar ratio of 1: 10: 15 and placed into an alumina crucible which was then sealed into a quartz tube in vacuum. The assembly was heated in a furnace up to 750 °C within 10 hrs, kept at the temperature for 15 hrs, and then slowly cooled down to 613 °C at a temperature decreasing rate of 2 °C/h. The excess melt components were removed at this temperature by quickly placing the assembly into a high-speed centrifuge and black crystals with shining surface in a typical dimension of $2 \times 2 \times 0.2 \text{ mm}^3$, shown by the insert picture as Figure S1(a).

The phase and quality of the single crystals used in this work were examined on

a Bruker D8 Venture single crystal X-ray diffractometer (SXRD) with Mo $K_{\alpha 1}$ ($\lambda = 0.71073 \text{ \AA}$) and Bruker D8 Advance powder X-ray diffractometer (PXRD) with Cu $K_{\alpha 1}$ ($\lambda = 1.54184 \text{ \AA}$) at 298 K. The PXRD data are presented in the main text. The SXRD diffraction patterns of MnSb_4Te_7 shown in Figures S1(b)-1(d) could be satisfyingly indexed on the basis of a trigonal structure with the lattice parameters with $a = b = 4.25 \text{ \AA}$, $c = 23.76 \text{ \AA}$, $\alpha = \beta = 90^\circ$ and $\gamma = 120^\circ$ in the space group $P\bar{3}m1$ (No. 164). The refinement results are summarized in Table S1. The perfect reciprocal space lattice indicates the high quality of our single crystal sample.

Table S1. Refinement results for MnSb_4Te_7 based on the single crystal x-ray diffraction data collected at room temperature.

Atom	site	x	y	z	U
Mn	1b	1	0	0	0.0171
Sb1	2d	0.3333	0.6667	0.4167	0.0424
Sb2	2d	0.3333	0.6667	0.1579	0.0469
Te1	1b	0	1	0.5	0.0362
Te2	2d	0.6667	0.3333	0.3457	0.0372
Te3	2c	0	1	0.2271	0.0369
Te4	2d	0.6667	0.3333	0.0711	0.0384

b. Magneto-transport measurements

The magnetizations were measured by using a commercial Magnetic Property Measurement System (MPMS-3). The alternating current magnetization was measured at the magnetic field $\mu_0 H = 10 \text{ Oe}$ and the frequency of 273Hz. Magnetotransport measurements, including the resistivity, magnetoresistance and Hall effect measurements, were carried out in commercial DynaCool Physical Properties

Measurement System from Quantum Design. The resistivity and magnetoresistance were measured in a four-probe configuration and the Hall effect measurement was using a standard six-probe method.

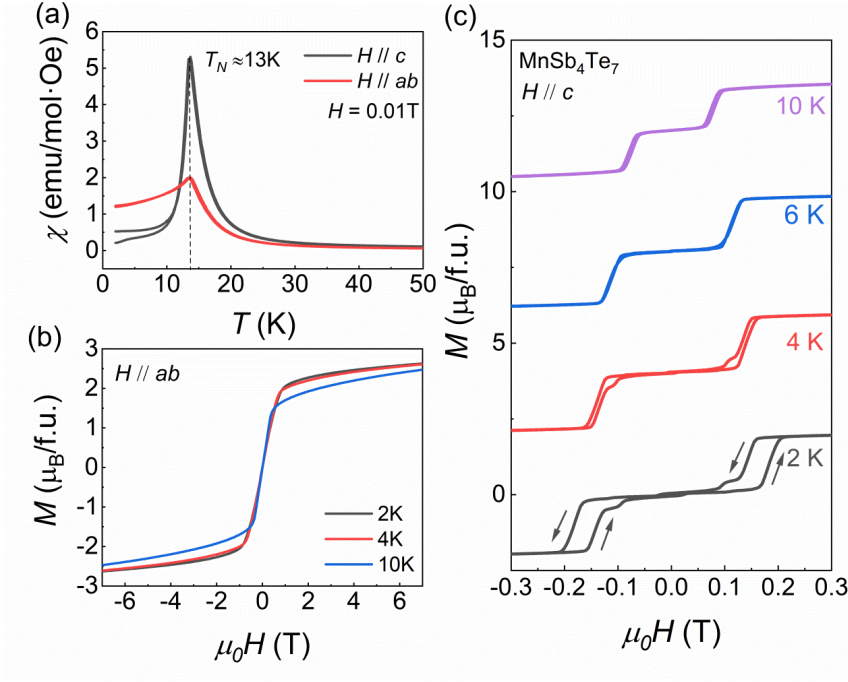


Fig. S2. (a) The temperature dependence of magnetic susceptibility χ under $\mu_0H = 0.01$ T for $H // c$ and $H // ab$ plane. (b) Isothermal magnetizations at 2 K, 4 K and 10 K for $H // ab$. (c) Isothermal magnetizations at 2 K, 4 K, 6 K and 10 K for $H // c$.

As mentioned in the main text, the intrinsic long range AFM order could be identified in the magnetic susceptibility curves. when $H // c$, the ZFC and FC curves separate slightly at low temperature, indicating the possibility of hysteresis loops, which could be further demonstrated by the hysteresis loops of isothermal magnetizations as shown in Figure S2(c), where a first-order spin flip transition with hysteresis at 2 K beginning at $\mu_0H = 0.16$ T and vanishing at $\mu_0H = 0.21$ T is visible. At $\mu_0H = 0.21$ T, the system enters into the forced FM state, which is similar as the case of MnBi_4Te_7 [1, 2]. Comparing with the MnSb_2Te_4 , the smaller saturation

magnetic field indicates the weaker Mn^{2+} - Mn^{2+} interlayer AFM exchange. While increasing the temperature to 10 K, the hysteresis loop gradually diminishes to be nearly zero, but the spin-flip transition is still observable below T_N . The saturation moment at 2 K under $\mu_0 H = 0.3$ T is $1.93\mu_B/\text{Mn}^{2+}$, which is smaller than the value of $3.5\mu_B/\text{Mn}^{2+}$ of MnBi_4Te_7 [1]. The reason may lie in that the Mn disorders and mixed location of Mn and Sb atoms [3], or due to the enhanced hole-carrier mediated Ruderman-Kittler-Kasuya-Yosida (RKKY) interaction which could give rise to magnetic frustration [4-6]. Figure S2(b) displays the isothermal magnetizations with $H // ab$, showing that the saturation field is about 1 T with the almost similar saturation moment, indicating that the c axis is the magnetic easy axis.

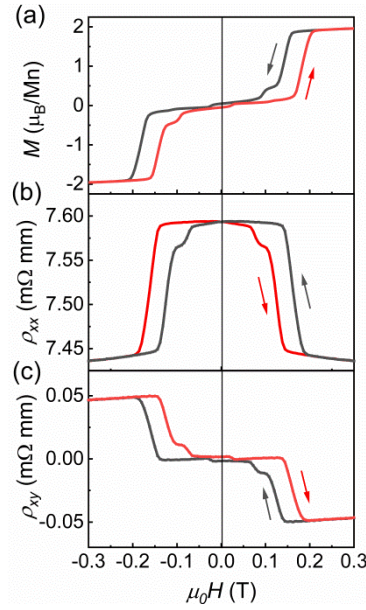


Fig. S3. Magnetotransport properties of bulk MnSb_4Te_7 single crystal. (a) The field dependence of magnetization M , (b) transverse magnetoresistance ρ_{xx} , and (c) Hall resistivity ρ_{xy} at 2 K with $H // c$ and $I // ab$ plane.

The magnetotransport properties are toughly related with the magnetic structure. For MnSb_4Te_7 , as displayed in Figure S3, $\rho_{xx}(H)$ and $\rho_{xy}(H)$ follow the same hysteresis loop as that in $M(H)$ with $H // c$ and $I // ab$ plane, where the red and black

arrows represent the paths for changing the magnetic field. The MnSb_4Te_7 single crystal used for the magnetotransport measurements has the thickness of ~ 0.1 mm. The magnetic field dependent $\rho_{xx}(H)$ and $\rho_{xy}(H)$ measured in the magnetic field range of $\mu_0 H = -1.5$ T $-$ 1.5 T are shown in Figures S4(a) and (b), respectively.

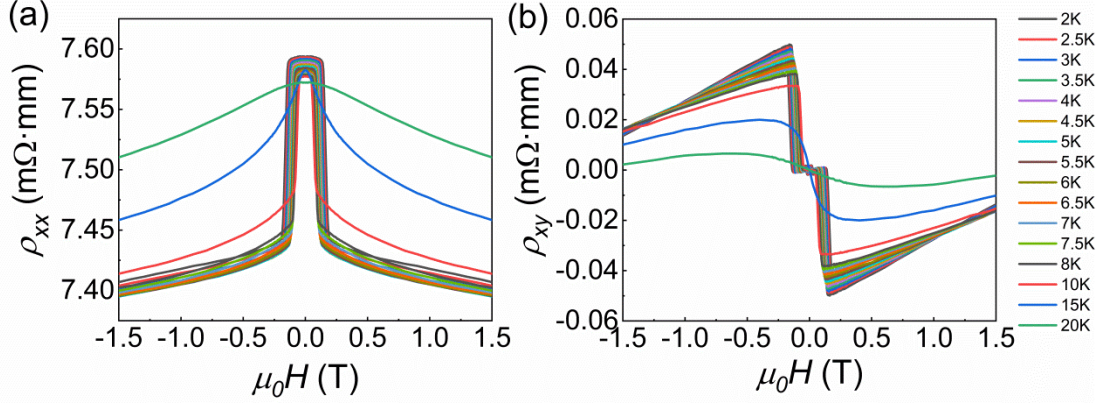


Fig. S4. Magnetotransport properties of bulk MnSb_4Te_7 single crystal. (a) Magnetoresistance ρ_{xx} with $I \parallel ab$ plane and $H \parallel c$ at various temperatures. (b) Hall resistivity ρ_{xy} measured at the same temperatures as in (a).

c. First-principle calculations

The first-principle calculations were carried out in the framework of the generalized gradient approximation (GGA) functional [7] of the density functional theory through employing the Vienna *ab initio* simulation package (VASP) [8] with projector augmented wave method [9]. The SOC effect was included in calculations. Considering the transitional metal Mn element, $U = 3$ eV are used in all calculations. The Bloch states are projected to the Wannier functions [10, 11] to build the tight-binding Hamiltonian, and then use *irvsp* program [12] and WannierTools package [13] to calculate the anomalous Hall conductivity.

We also consider the slab with few layers which keep antiferromagnetic and have two same terminations, and their energy bands are present in the Figure S7. We can see the band gap of about 20 meV will disappear while the thickness of antiferromagnetic slab is changed from five layers to nine layers.

Table S2. The numbers of occupied states with even/odd parity at the inversion-invariant momenta of bulk MnSb_4Te_7 at the four different magnetic states.

Time-reversal invariant momenta	Number of occupied bands with even parity (+)	Number of occupied bands with even parity (-)
AFM		
(0,0,0)	76	74
(1/2,0,0), (0,1/2,0), (1/2,1/2,0)	74	76
(0,0,1/2)	75	75
(1/2,0,1/2), (0,1/2,1/2), (1/2,1/2,1/2)	75	75
FMz		
(0,0,0)	37	38
(1/2,0,0), (0,1/2,0), (1/2,1/2,0)	35	40
(0,0,1/2)	39	36
(1/2,0,1/2), (0,1/2,1/2), (1/2,1/2,1/2)	39	36
FMx		
(0,0,0)	37	38
(1/2,0,0), (0,1/2,0), (1/2,1/2,0)	35	40
(0,0,1/2)	39	36
(1/2,0,1/2), (0,1/2,1/2), (1/2,1/2,1/2)	39	36
FMy		
(0,0,0)	37	38
(1/2,0,0), (0,1/2,0), (1/2,1/2,0)	35	40
(0,0,1/2)	39	36
(1/2,0,1/2), (0,1/2,1/2), (1/2,1/2,1/2)	39	36

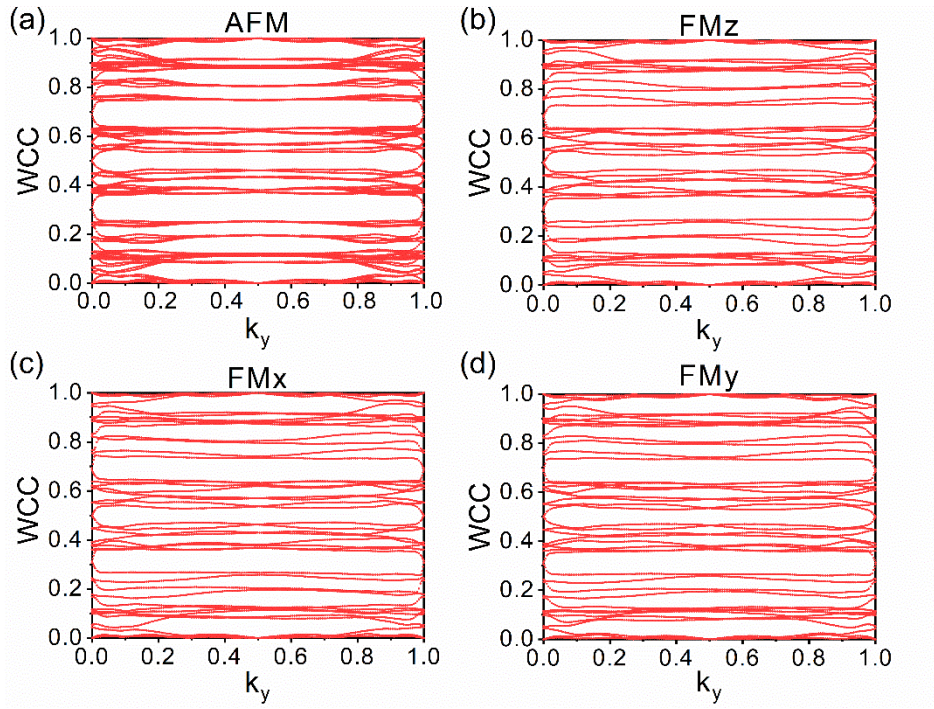


Fig. S5. The Wannier charge center (WCC) evolution in four magnetic states in the $k_z = 0$ plane.

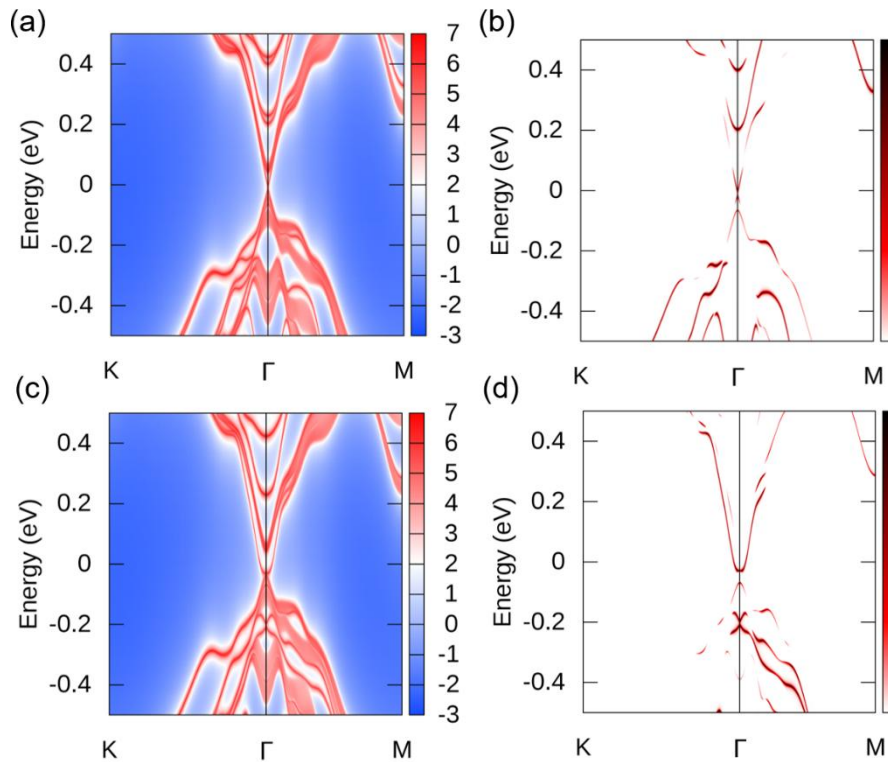


Fig. S6. (a) The calculated k-E map of MnSb_4Te_7 with the MnSb_2Te_4 SL termination. The spectrum of only surface states is present in the (b). (c) The calculated k-E map of MnSb_4Te_7 with the Sb_2Te_3 QL termination. The spectrum of only surface states is in the (d).

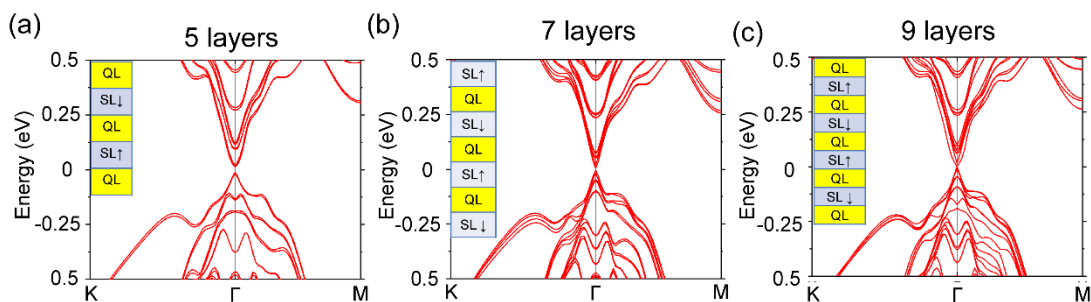


Fig. S7. The calculated energy bands of various few layers of MnSb_4Te_7 in the AFM configurations.

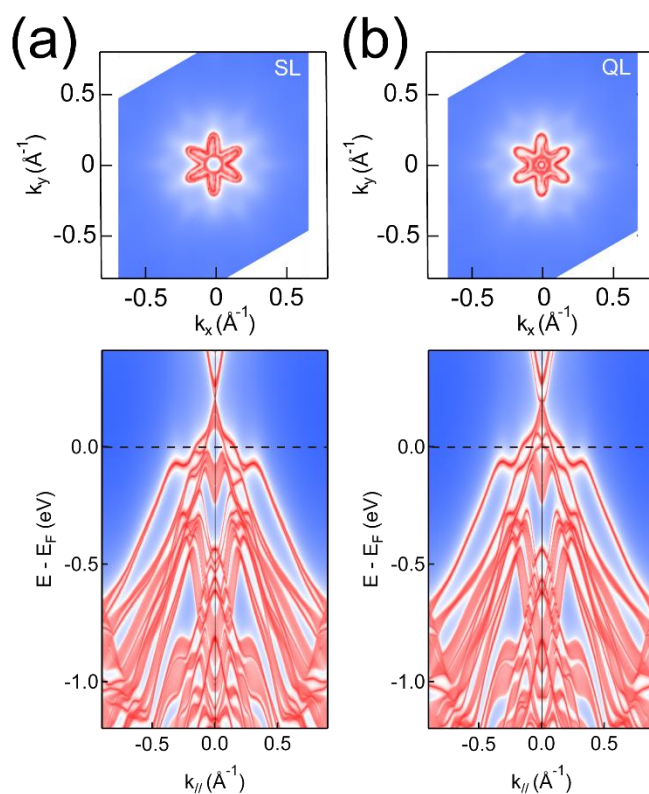


Fig. S8. Calculated Fermi surface and band structure of MnSb_4Te_7 system with (a) SL and (b) QL terminations. The directions of the energy bands are along $-\text{K}-\Gamma-\text{K}$.

d. The ARPES measurements

ARPES measurements were performed at beam line 03U of Shanghai Synchrotron Radiation Facility (SSRF). The samples were cleaved in situ and measured under ultrahigh vacuum below 8×10^{-11} Torr. Data were collected by Scienta DA30 analyzer. The total energy resolutions are 15 ~ 18 meV with photon energy 50 ~ 90 eV and angle resolution is 0.2° .

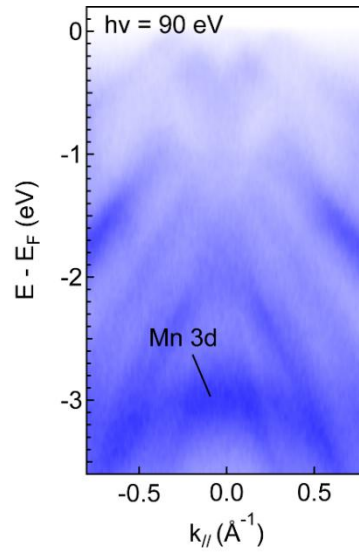


Fig. S9. Valence band structure of MnSb_4Te_7 collected at 15 K with photon energy of 90 eV.

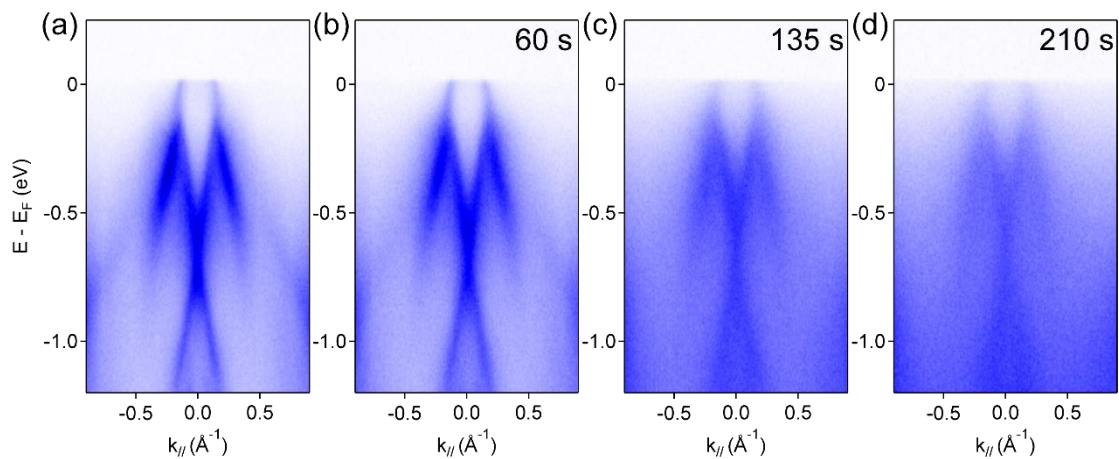


Fig. S10. ARPES intensity map of potassium doped MnSb_4Te_7 with different time: (a) 0s; (b) 60s;

(c) 135s; (d) 210s.

References

- [1] C. Hu, K. N. Gordon, P. Liu, J. Liu, X. Zhou, P. Hao, D. Narayan, E. Emmanouilidou, H. Sun, Y. Liu, H. Brawer, A. P. Ramirez, L. Ding, H. Cao, Q. Liu, D. Dessau, and N. Ni, *Nat. Commun.* **11**, 97 (2020).
- [2] J. Wu, F. Liu, M. Sasase, K. Ienaga, Y. Obata, R. Yukawa, K. Horiba, H. Kumigashira, S. Okuma, T. Inoshita, and H. Hosono, *Sci. Adv.* **5**, eaax9989 (2019).
- [3] T. Murakami, Y. Nambu, T. Koretsune, G. Xiangyu, T. Yamamoto, C. M. Brown, and H. Kageyama, *Phys. Rev. B* **100**, 195103 (2019).
- [4] M. A. Ruderman and C. Kittel, *Phys. Rev.* **96**, 99 (1954).
- [5] K. Yosida, *Phys. Rev.* **106**, 893 (1957).
- [6] T. Kasuya, *Progress of Theoretical Physics* **16**, 45 (1956).
- [7] J. P. Perdew, K. Burke, and M. Ernzerhof, *Phys. Rev. Lett.* **77**, 3865 (1996).
- [8] G. Kresse and J. Hafner, *Phys. Rev. B* **47**, 558 (1993).
- [9] P. E. Blöchl, *Phys. Rev. B* **50**, 17953 (1994).
- [10] A. A. Mostofi, J. R. Yates, Y.-S. Lee, I. Souza, D. Vanderbilt, and N. Marzari, *Comput. Phys. Commun.* **178**, 685 (2008).
- [11] N. Marzari, A. A. Mostofi, J. R. Yates, I. Souza, and D. Vanderbilt, *Rev. Mod. Phys.* **84**, 1419 (2012).
- [12] J. Gao, Q. Wu, C. Persson, Z. Wang, *Comput. Phys. Comm.* **261**, 107760 (2021).
- [13] Q. S. Wu, S. N. Zhang, H. F. Song, M. Troyer, A. A. Soluyanov, *Comput. Phys. Commun.* **224**, 405 (2018).